Evolution of ground state in Cr_2Te_3 single crystal under applied magnetic field

Z. Z. Jiang,[1,2,*] X. Liang,[1,2,*] X. Luo,[1,†] J. J. Gao,[1,2] W. Wang,[1,2] T. Y. Wang,[1,2] X. C. Yang,[1,2] X. L. Wang,[1,2] L. Zhang,[3] Y. Sun,[4] P. Tong,[1] J. F. Hu,[5,6] W. H. Song,[1] W. J. Lu,[1,‡] and Y. P. Sun[3,1,7,§]

[1]*Key Laboratory of Materials Physics, Institute of Solid State Physics, HFIPS, Chinese Academy of Sciences, Hefei 230031, China*

[2]*Island Branch of Graduate School, University of Science and Technology of China, Hefei 230026, China*

[3]*Anhui Province Key Laboratory of Condensed Matter Physics at Extreme Conditions, High Magnetic Field Laboratory, HFIPS, Chinese Academy of Sciences, Hefei 230031, China*

[4]*Institutes of Physical Science and Technology, Anhui University, Hefei 230601, China*

[5]*Laboratory of Magnetic and Electric Functional Materials and the Applications, Key Laboratory of Shanxi Province, Taiyuan 030024, China*

[6]*College of Materials Science & Engineering, Taiyuan University of Science and Technology, Taiyuan 030024, China*

[7]*Collaborative Innovation Center of Advanced Microstructures, Nanjing University, Nanjing 210093, China*

(Received 7 August 2021; revised 19 August 2022; accepted 24 August 2022; published 6 September 2022)

Two-dimensional magnetic materials hold great promise for applications toward efficient data storage and transfer. It would be a huge advantage if their ground-state properties had strong responses against external stimulations, such as magnetic and electric fields. Here, we report several intriguing discoveries in single-crystal Cr_2Te_3. Based on comprehensive specific heat, differential scanning calorimetry, variable-temperature x-ray diffraction, and linear-thermal-expansion measurements, we find that Cr_2Te_3 has a low-temperature ferromagnetic (FM) ground-state phase, which changes to an antiferromagnetic (AFM) phase when temperature is increased to $T_C = 160$ K. This FM-AFM transition is a first-order phase transition, and the transition temperature can be further enhanced to 178 K by a moderate magnetic field. At the same time, the first-order phase transition will transform into a second-order phase transition, indicating strong spin-lattice coupling (SLC). A second-order AFM-paramagnetic phase transition emerges at $T_N = 181$ K. This AFM phase is gradually suppressed by the magnetic field and eventually disappears at a critical field of 0.48 T. The SLC results in a notable negative-thermal-expansion coefficient of -17.2 ppm/K and a remarkable magnetostriction coefficient of 44.7 ppm/T at 200 K. With the assistance of first-principles density functional theory calculations and Monte Carlo simulations, we conclude that the collinear FM, canted FM, and AFM configurations in Cr_2Te_3 depend on the temperature and applied magnetic field. Our work reveals the highly tunable magnetic phases and SLC in Cr_2Te_3, which will be helpful for developing the potential functionalities of this material.

DOI: 10.1103/PhysRevB.106.094407

I. INTRODUCTION

Two-dimensional (2D) magnetic materials have recently received increased attention. Besides being ideal experimental platforms for many magnetic exchange interaction models, they have potential applications in spintronics devices. Magnetic anisotropy in 2D materials has long been theorized to enable long-range magnetic ordering, forming 2D magnets [1]. Recently, such devices were experimentally confirmed with the discovery of monolayer CrI_3 and bilayer $Cr_2Ge_2Te_6$, with Curie temperatures T_C of only 45 K [2] and 30 K [3], respectively. Monolayer Fe_3GeTe_2 ($T_C = 20$ K) uses an ionic gate method, and its T_C could be raised to room temperature [4]. The search for high-temperature 2D magnetic materials has been intense, involving theoretical and experimental efforts. The research work has also seriously considered transition metal dichalcogenides. Monolayer VSe_2 has been successfully grown via the molecular beam epitaxy method [5], which can maintain a robust ferromagnetic (FM) behavior with a large magnetic moment above room temperature even if it is chemically unstable. Yu *et al.* [6] reported that introducing thiol molecules onto the VSe_2 surface could passivate the exfoliated flakes, thus well addressing the instability problem. In the monolayer limit, epitaxial $MnSe_2$ also exhibits room-temperature ferromagnetism [7]. For TaS_2, magnetic ion intercalated $Mn_{0.25}TaS_2$ and $Fe_{0.25}TaS_2$ thin films can both have long-range FM orders [8]. Two-dimensional magnetic materials present formidable challenges due to their low Curie temperature and instability. Researchers have recently turned their attention to metal tellurides, specifically Cr-based Te compounds.

Chromium tellurides $Cr_{1+x}Te_2$ ($-0.333 \leqslant x \leqslant 1$) exhibit a wide variety of structural, electrical, and magnetic properties due to their rich physical phases and tunability. According to previous reports [9–19], this compound has been fabricated in more than 10 compositional variants, ranging from $CrTe_3$ ($x = -0.333$) to CrTe ($x = 1$), with the proportion of Cr changing from less to more. Interestingly, within each of the phases, it again varies with the difference in low Cr concentration, as ultimately expressed in the magnetism and resistivity. $CrTe_2$, a quasi-2D van der Waals (vdW) material, was first prepared in bulk using rapid precipitation in solution

*These authors contributed equally to this work.
†Corresponding author: xluo@issp.ac.cn
‡wjlu@issp.ac.cn
§ypsun@issp.ac.cn

with T_C of 350 K [11]. Freitas *et al.* [20] also synthesized it indirectly by oxidizing $KCrTe_2$, obtaining T_C of 310 K. Sun *et al.* [21] first demonstrated that ferromagnetism could hold above 300 K in 1*T*-$CrTe_2$ down to the ultrathin limit, making it an exfoliated ultrathin vdW magnet with intrinsic long-range magnetic ordering above room temperature. Wen *et al.* [22] reported a breakthrough by synthesizing one- and two-unit-cell Cr_2Te_3 ($x = 0.333$) and discovering near-room-temperature ferromagnetism in 2D Cr_2Te_3. In contrast to $CrTe_2$, the dimensional effect of Cr_2Te_3 was more prominent, where its T_C ranged from 160 to 280 K, with the thickness changing from 40 down to 5 nm [22,23]. So far, Cr_2Te_3 thin films have been extensively studied both theoretically and experimentally, including as novel heterojunction devices [24,25] and topological Hall effect devices [26–28]. However, relatively little research has been carried out on Cr_2Te_3 single crystals so far. The intrinsic and detailed properties of Cr_2Te_3 remain unclear. Consequently, one of the motivations of this work is to better understand the bulk properties of Cr_2Te_3.

In this work, we grew Cr_2Te_3 single crystals and performed comprehensive investigations of their response to an external magnetic field. A field-controlled first-order FM-antiferromagnetic (AFM) phase transition with a strong spin-lattice-coupling (SLC) effect was observed. Upon applying a moderate magnetic field, the first-order phase transition transformed into a second-order phase transition. Moreover, the magnetic field enhanced the FM transition temperature considerably, with T_C changing from 160 to 178 K. The second-order AFM transition initially appeared at $T_N = 181$ K, with the temperature decreasing as the field strength increased, until this transition eventually disappeared. The linear-thermal-expansion measurements directly presented the relevance of the structure versus the applied magnetic field and temperature, with a large negative thermal expansion (NTE) coefficient of $\alpha_L = -17.2$ ppm/K in the *ab* plane. First-principles calculations yielded a possible magnetic structure for the ground state and revealed the characteristics of different magnetic interactions. We ascribed these findings to the canted FM structure and strong SLC in Cr_2Te_3. Finally, the *H*–*T* phase diagram was obtained using the critical fields deduced from Arrott plots. We expect these investigations to contribute to a better understanding of the critical behavior and magnetic interactions of 2D magnetic materials with multiple phase transitions. Furthermore, the strong SLC in Cr_2Te_3 represents a development toward future spintronics devices.

II. METHODS

Single crystals of Cr_2Te_3 were grown using the self-flux method. Cr powder (99.94%, Alfa Aesar) and Te chunks (99.999%, Aladdin) were mixed in a ratio of 1:4 and sealed in an evacuated quartz tube. The quartz tube was heated up to 1473 K at a rate of 60 K/h, equilibrated for 12 h, and then slowly cooled at a rate of 2 K/h. After reaching 1153–1183 K, it was taken out quickly from the furnace and decanted with a centrifuge to separate the single crystals from the Te flux. X-ray diffraction (XRD) patterns of single crystals and polycrystalline powders, crushed from the single crystals, were measured by a PANalytical X'Pert diffractometer using the Cu $K\alpha$ radiation (1.5406 Å) at room temperature. The synchrotron x-ray powder diffraction measurements were performed at room temperature using the powder diffractometers on beamlines 02U (0.58490 Å) at the Shanghai Synchrotron Radiation Facility, Shanghai. The atomic ratio was determined by the Aztec-X-Max 80 energy dispersive x-ray spectrometer in the Hitachi SU8000 series scanning electron microscope (see Fig. S1 in the Supplemental Material [29]). The detailed information of the structure transition was studied by variable-temperature XRD measurements using a Rigaku-D/max-γ A diffractometer employing high-intensity Cu $K\alpha$ radiation from 300 to 20 K. Magnetic measurements were performed on a Quantum Design magnetic property measurement system (MPMS-XL5). The resistivity, specific heat, and linear thermal expansion $\Delta L/L$ (using a strain gauge) data were collected in the temperature range from 300 to 2 K using a Quantum Design physical property measurement system (PPMS-9T). Differential scanning calorimetry (DSC) measurements were carried out on a sample of ~6.9 mg using a TA instruments 200 F3 equipped with a refrigerated cooling system under N_2 atmosphere. The sample was cooled down to 100 K, followed by heating from 100 K to room temperature at the scanning rate of 10 K/min.

Our first-principles calculations based on the density functional theory (DFT) [30] were implemented in the Vienna Ab initio Simulation Package (VASP) [31,32], and the generalized gradient approximation [33] according to the Perdew-Burke-Ernzerhof parametrization was used. The projector augmented wave [34] method was employed to simulate the ionic potentials. We set a plane-wave kinetic cutoff energy of 400 eV for all calculations. The system was fully optimized in regard to the atomic positions until the force and energy converged to 0.01 eV/Å and 10^{-5} eV, respectively. We used the $4 \times 4 \times 2$ *k*-point sampling for the Brillouin zone integration. We considered spin-orbit coupling in the calculation. For magnetic systems, the Hamiltonian based on the Wannier function was constructed using WANNIER90 [35]. Then, we used the TB2J package [36] to calculate the exchange parameters.

III. RESULTS AND DISCUSSION

Figure 1(a) shows that Cr_2Te_3 crystallized as almost hexagonal flakes. The XRD pattern of the single crystal showed that the natural surface is the (00*l*) plane. This crystal structure is closely linked to $CrTe_2$, with every two layers of supercells ($\sqrt{3} \times \sqrt{3}$) intercalated by one Cr atom. To characterize this structure, crushed Cr_2Te_3 single crystals were analyzed via powder XRD at room temperature. XRD refinement data [Fig. 1(b)] indicate that Cr_2Te_3 has a trigonal crystal structure with space group $P\bar{3}1c$ (No. 163), and the derived lattice constants are $a = b = 6.7921(2)$ Å and $c = 11.985(2)$ Å. We find an additional minor peak contributed by a small amount of the remaining Te flux between the (110) and (004) peaks. Previous reports indicated that XRD patterns of the variants of $Cr_{1+x}Te_2$ are very similar, and the low-symmetry phases usually have a split XRD peak around scattering angles of 50° (Cu $K\alpha$) [37]. A high-resolution XRD measurement did not find such a split peak (see Fig. S2 in the Supplemental Material [29]), confirming the Cr_2Te_3 phase of our single crystals.

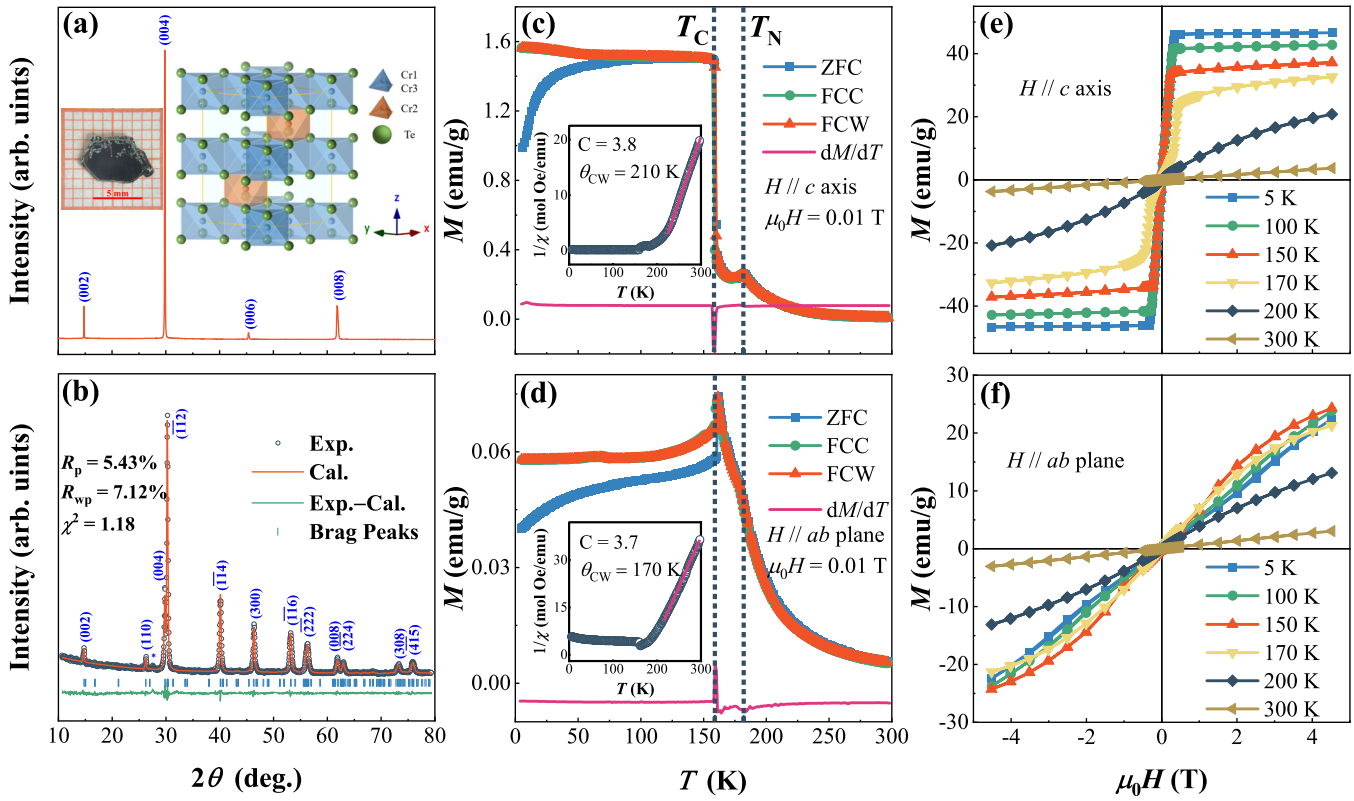

FIG. 1. (a) X-ray diffraction pattern of single-crystalline Cr_2Te_3 showing $(00l)$ diffraction peaks. The schematic insets show Cr_2Te_3 morphology and structure. (b) Powder XRD pattern of crushed Cr_2Te_3 single crystals measured at room temperature. (c) and (d) Temperature dependence of magnetization $M(T)$ under ZFC, FCC, and FCW modes with H along the c axis and the ab plane, respectively. T_C was defined as the temperature of the minimum slope of the $M(T)$ curve under the ZFC mode. T_N was defined as the temperature of the local maximum of the $M(T)$ curve under the ZFC mode. The insets show the temperature-dependent inverse susceptibility $1/\chi(T)$ of Cr_2Te_3 in 0.01 T with H along the c axis and the ab plane, respectively. The pink solid lines were the fitted results according to the Curie-Weiss law. (e) and (f) Magnetic field dependence of magnetization $M(H)$ at 5, 100, 150, 170, 200, and 300 K for Cr_2Te_3 single crystals. The applied magnetic field was along the c axis and the ab plane, respectively.

To explore the crystal's magnetism, its temperature-dependent magnetizations $M(T)$ along the c axis and the ab plane were measured. Figures 1(c) and 1(d) showed $M(T)$ curves of Cr_2Te_3 in the zero-field-cooled (ZFC), field-cooled-cooling (FCC), and field-cooled-warming (FCW) modes of Cr_2Te_3 in a 0.01 T magnetic field ($\mu_0 H$). For both directions, we found kinks on $M(T)$ curves at 181 K, denoted as T_N, which could be attributed to the AFM-paramagnetic (PM) transition, and rapid changes at around 160 K, denoted as T_C, may be attributed to the FM-AFM transition, both of which were confirmed by the anomalies of derivatives dM/dT. This is consistent with previous observations in ultrathin Cr_2Te_3 films [22,38]. The large difference in magnetization along the two measured directions is evidence of strong magnetic anisotropy in single-crystal Cr_2Te_3. The insets of Figs. 1(c) and 1(d) depict that the temperature-dependent inverse susceptibility $1/\chi$ above T_C can be described well by the Curie-Weiss law from the mean-field theory [39]:

$$\frac{1}{\chi} = \frac{T - \theta_{CW}}{C}, \tag{1}$$

where C is the Curie constant and θ_{CW} is the Curie-Weiss temperature. The fitted C values are 3.8 (c axis) and 3.7 (ab plane), and the effective magnetic moment μ_{eff} is determined to be around $3.90\mu_B$, which is close to the theoretical value of 3.87 expected for Cr^{3+} according to the equation calculated from the ionic model, $\mu_{eff} = \sqrt{3k_B C/N_A}\mu_B$. However, the ordered magnetic moment of a Cr atom derived from saturation magnetization is about $2.04\mu_B$, consistent with a previous report [40], but is much smaller than the μ_{eff} calculated using the Curie-Weiss law, indicating the itinerancy of $3d$ electrons [41]. The Curie-Weiss temperatures θ_{CW} were positive for both directions, suggesting that FM exchange interactions dominated in both directions. θ_{CW} for $H \parallel c$ axis (210 K) is much higher than that for $H \parallel ab$ plane (170 K), indicating the existence of AFM interactions. Figures 1(e) and 1(f) present measurements of isothermal magnetic susceptibility. The magnetization along the c direction is easier to saturate than the case in the ab plane, indicating that the c axis is the easy magnetization axis. This result is similar to that for other chromium tellurides, e.g., Cr_5Te_8 [42]. Simultaneously, a slight metamagnetic transition apparently occurred at 170 K, which is just between T_C and T_N.

The crystal's magnetic anisotropy was thoroughly investigated by measuring angle-dependent magnetization $M(\varphi)$. As depicted in Figs. 2(a)–2(d), the $M(\varphi)$ curves have simple twofold symmetries at 5 and 150 K, indicating a uniaxial anisotropy along the c axis. As the magnetic field strength

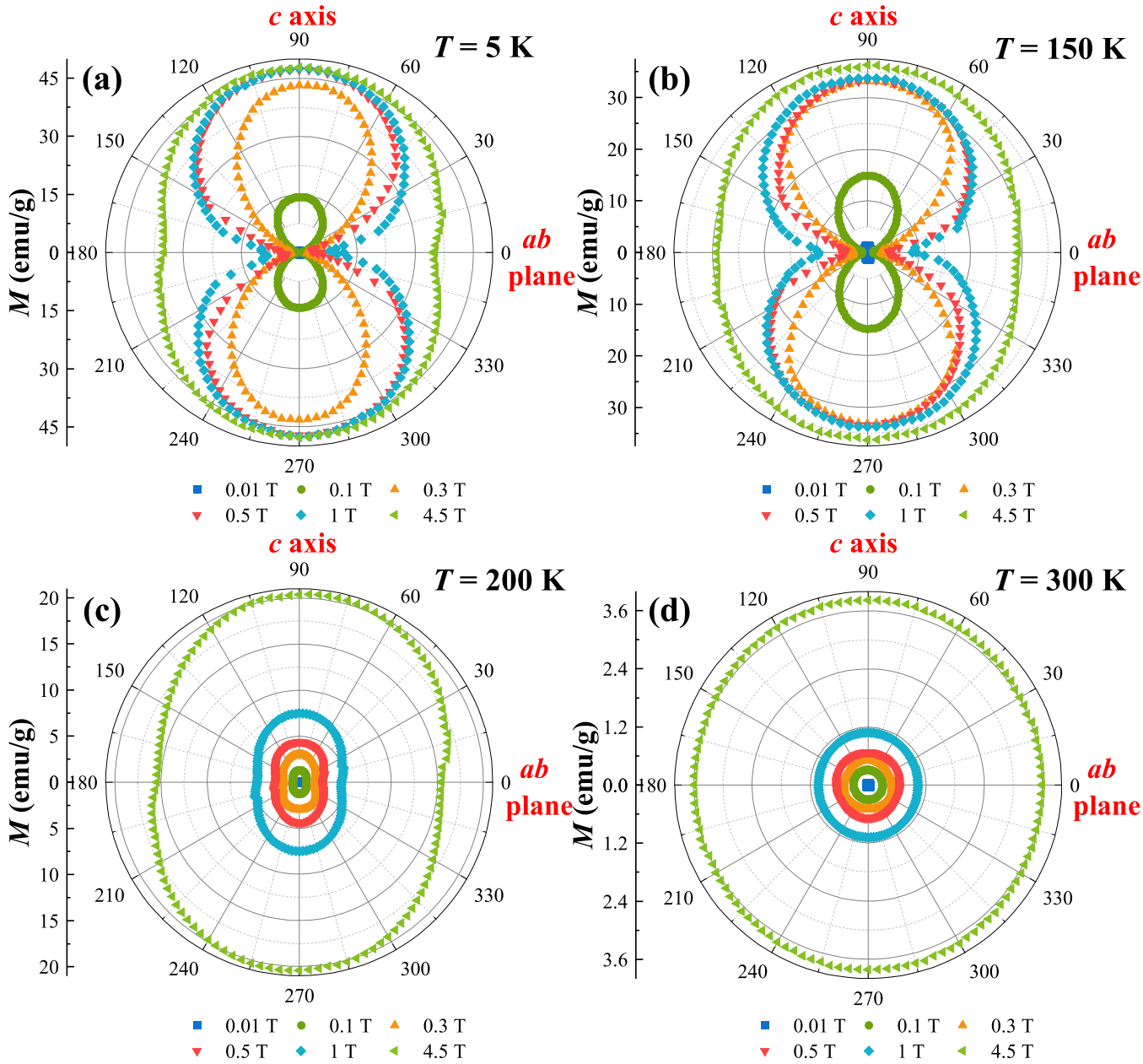

FIG. 2. The angle-dependent magnetization at $T = 5$, 150, 200, and 300 K. The applied magnetic fields are 0.01, 0.1, 0.3, 0.5, 1, and 4.5 T, respectively.

increases, the anisotropy diminishes significantly, with the curves gradually becoming oval as $\mu_0 H$ approaches 1 T. Above the AFM phase transition temperature, the magnetic anisotropy changes significantly since the magnetic interactions disappear at this point and the thermal perturbations lead to a spatially isotropic spin arrangement. At room temperature, $M(\varphi)$ forms several concentric curves in different fields, indicating homogeneity in all directions. Meanwhile, the magnetic anisotropy of Cr_2Te_3 also behaves as the anisotropy of the magnetocaloric effect (see Fig. S3 in the Supplemental Material [29]).

To investigate the evolution of the phase transitions under external fields, $M(T)$ measurements in various fields for $H \parallel c$ axis were carried out. Figure 3(a) illustrates that the applied field significantly raised T_C from 160 to 178 K when $\mu_0 H =$ 1 T while also lowering T_N. The anomaly corresponding to the AFM-PM phase transition in the $M(T)$ curve disappears when $\mu_0 H \geqslant 0.5$ T, indicating the AFM phase is completely suppressed by this field. The resultant magnetic phase diagram is presented in Fig. 3(b).

To study the spin-dependent transport properties of Cr_2Te_3, the in-plane ($I \parallel ab$ plane) and out-of-plane ($I \parallel c$ axis) resistivities ρ were measured and are presented in Fig. 3(c). Both exhibit metallicity with temperatures ranging from 2 to 300 K. A clear discontinuous change corresponding to the FM-AFM transition occurs at about 160 K, consistent with the measurements. The ρ measured along different directions are at the same magnitude as $\rho_c/\rho_{ab} = 1.6$ at 300 K, illustrating the three-dimensional electrical transport property in Cr_2Te_3. A notable thermal hysteresis of the cooling and warming

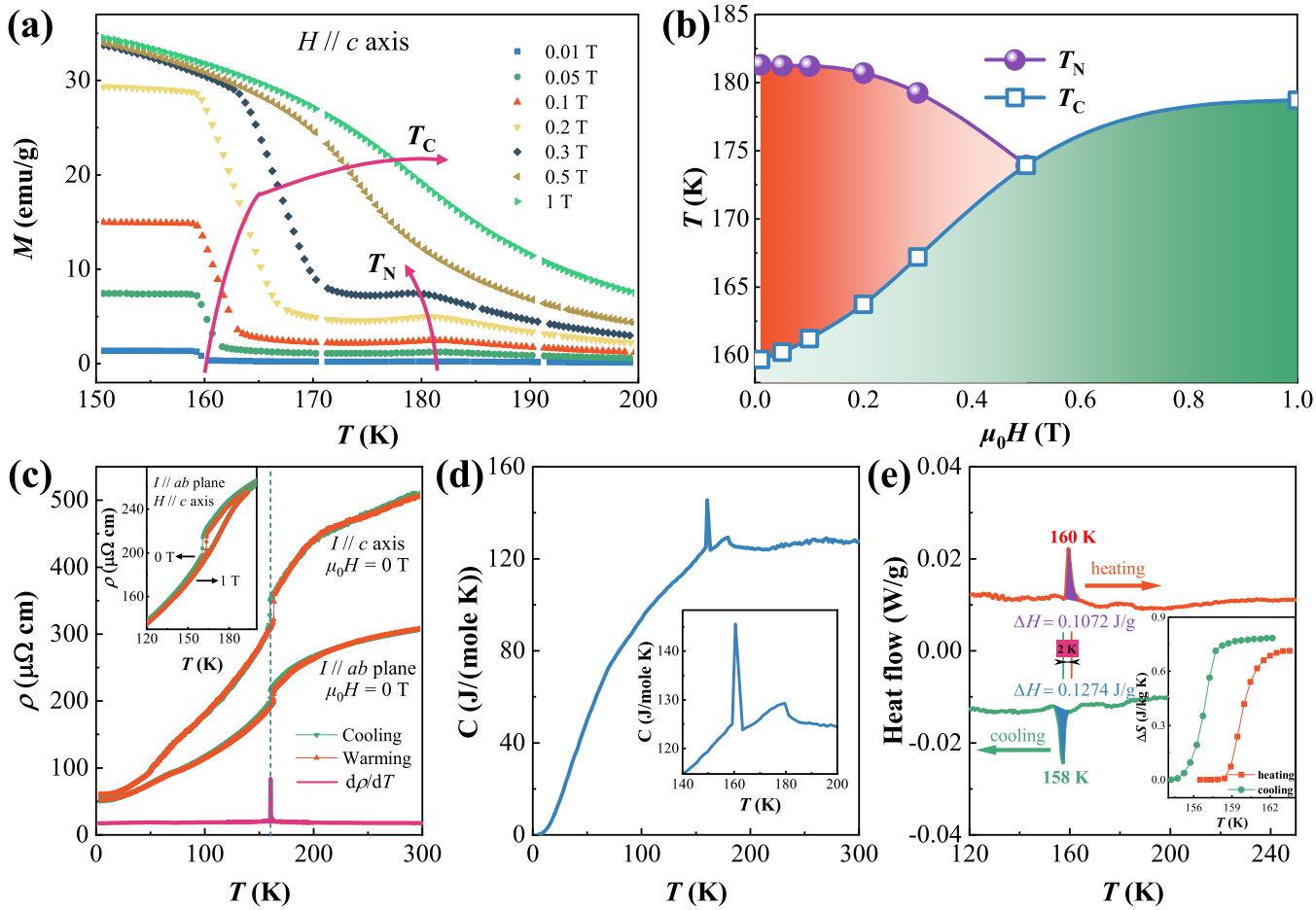

FIG. 3. (a) Magnetization as a function of temperature in various fields: 0.01, 0.05, 0.1, 0.2, 0.3, 0.5, and 1 T. (b) *T*-*H* phase diagram derived from (a). (c) Temperature dependence of in-plane and out-of-plane resistivity of Cr_2Te_3. Red and green lines represent warming and cooling curves, respectively. The inset shows the results before and after applying the field. (d) Specific heat C_p as a function of temperature T for Cr_2Te_3. (e) Heat flow dQ/dT on cooling (green) and heating (red) processes across the transition range. The inset is the resulting entropy change $\Delta S(T)$ with respect to T.

$\rho(T)$ curves is found around T_C, implying a first-order phase transition. The insets of Fig. 3(c) present $\rho(T)$ curves for $I \parallel ab$ plane and $\mu_0 H = 0$ and 1 T along the c direction. A negative magnetoresistance is observed, originating from the suppression of electron-magnon scattering by the magnetic field. Moreover, we find that the thermal hysteresis disappears when $\mu_0 H = 1$ T. This phenomenon indicates that a strong magnetic field suppresses the first-order phase transition and transforms it into a second-order phase transition.

The thermal effect accompanying the phase transition in Cr_2Te_3 is elucidated by specific heat and DSC measurements. Figure 3(d) displays two specific heat peaks appearing at T_C and T_N. The peak at T_C is sharp, implying that it is a first-order phase transition, while the peak at T_N is much broader, signifying a likely second-order phase transition. Figure 3(e) shows DSC curves with two distinct peaks in heating and cooling processes, directly confirming the nature of the first-order transition around T_C. No such peaks form around T_N, which also confirms a second-order phase transition at this temperature. The peaks positions, usually taken to be the phase transition temperature, are at 158 and 160 K, which translates to a small hysteresis of 2 K. After subtracting the baselines, the peak areas are integrated to obtain the enthalpy of transition ΔH and the entropy of transition ΔS [43]:

$$\Delta S = \int_{T_1}^{T_2} \frac{1}{T}\frac{dQ}{dT}dT = \int_{T_1}^{T_2} \frac{1}{T}\frac{\dot{Q}}{\dot{T}}dT, \tag{2}$$

where T_1 and T_2 are the start and end temperatures of the transition, respectively. We obtain $\Delta H = 0.11 \pm 0.1$ J/g and $\Delta S = 0.75 \pm 0.05$ J/K/kg from the inset of Fig. 3(e), indicating a weak first-order phase transition releasing a small amount of heat.

Figure 4(a) presents the variable-temperature XRD patterns captured as the crystal sample was cooled from 300 to 20 K. There are three Cu peaks and one Te peak. The former is from the Cu powder added to calibrate the crystal lattice, and the latter comes from the Te grains attached to the Cr_2Te_3 surface; they were ground together into a polycrystal. The diffraction peaks at different temperatures appear to be similar, indicating no change in the space group. However, as shown in Fig. 4(b), (004) and $(\bar{1}\bar{1}2)$ crystal planes gradually coalesce, implying an NTE of in-plane lattice constant a and a positive thermal expansion (PTE) of the out-of-plane lattice constant c. We plot the contour map of diffraction intensity as a function of temperature (from 300 to 20 K) and degree (from

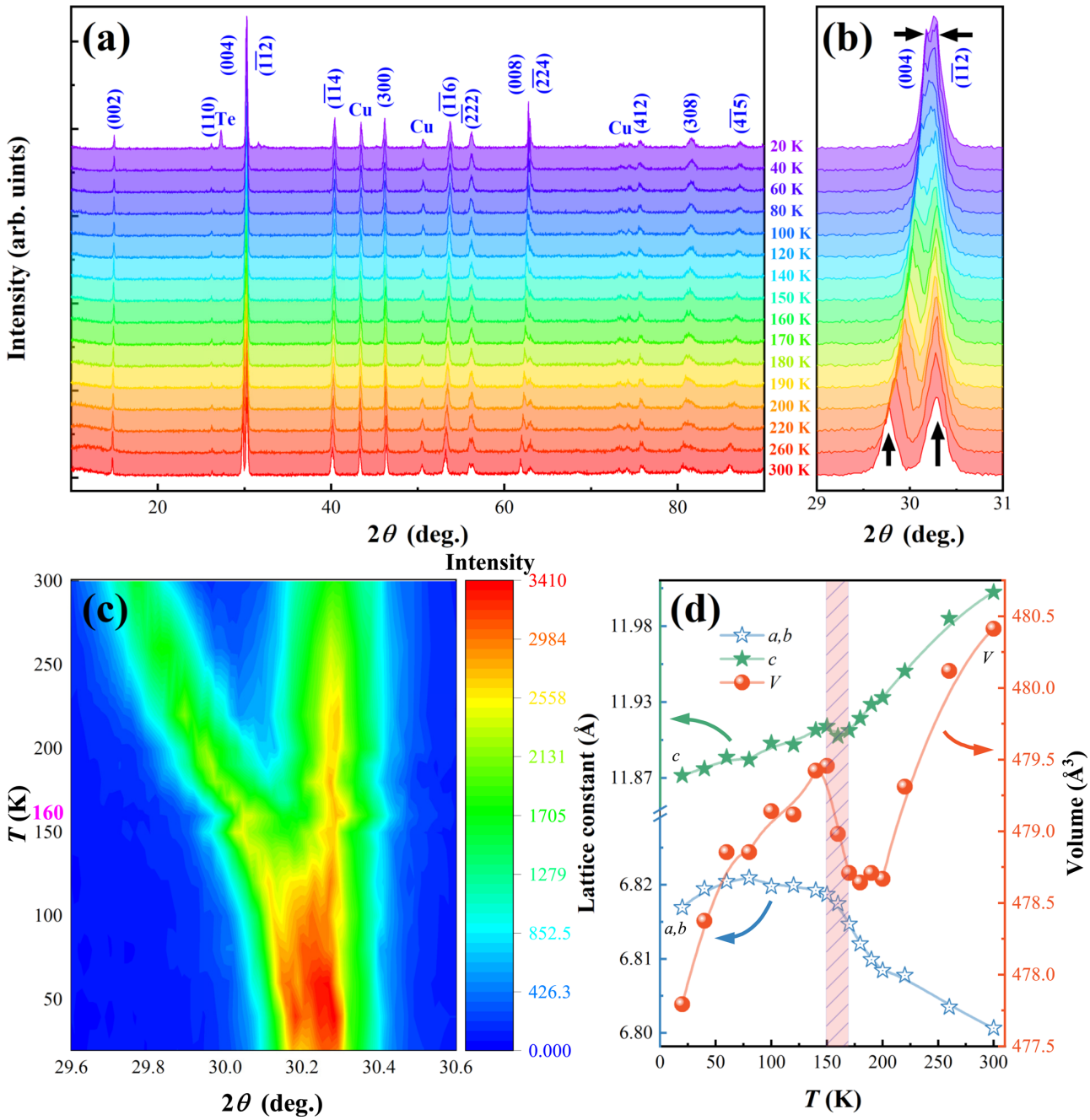

FIG. 4. (a) and (b) Variable-temperature x-ray diffraction patterns upon cooling from 300 to 20 K. (c) Contour plots of the (004) and ($\overline{1}\overline{1}2$) crystallographic planes. XRD profile intensity as a function of temperature and degree. (d) Lattice constants a, b, and c and unit cell volume V as a function of temperature.

29.6° to 30.6°). Above T_C, two areas with high diffraction intensity merge at about 30.1°, forming a Y-shaped pattern. This anomaly signifies that the lattice is distorted by the FM-AFM phase transition.

To confirm our conjecture, we performed the Rietveld refinement of XRD patterns at each temperature. Figure 4(d) displays the change in lattice constants a or b and c and the unit cell volume V in regard to temperature. First, the c axis exhibits a PTE, consistent with the results of the contour map. On the contrary, the a or b axis exhibits an NTE behavior in a wide temperature range. Around T_C, the c axis suddenly increases, but no obvious change is observed on the a or b axis, consistent with our resistance measurements, where the change in ρ in the c direction is more prominent than along the ab plane. The change in V can be calculated from a, b, and c. We observe an NTE of volume around the phase transition, while a normal PTE of volume remains for other temperatures.

NTE materials can be used to cancel out the normal PTE of most materials and thus have many potential applications. Figure 5(a) depicts the linear-thermal-expansion coefficient $\alpha_L = \Delta L/L$ along the ab plane for the Cr_2Te_3 single crystal obtained through the strain gauge method. The lattice constant a or b increases with decreasing temperature over

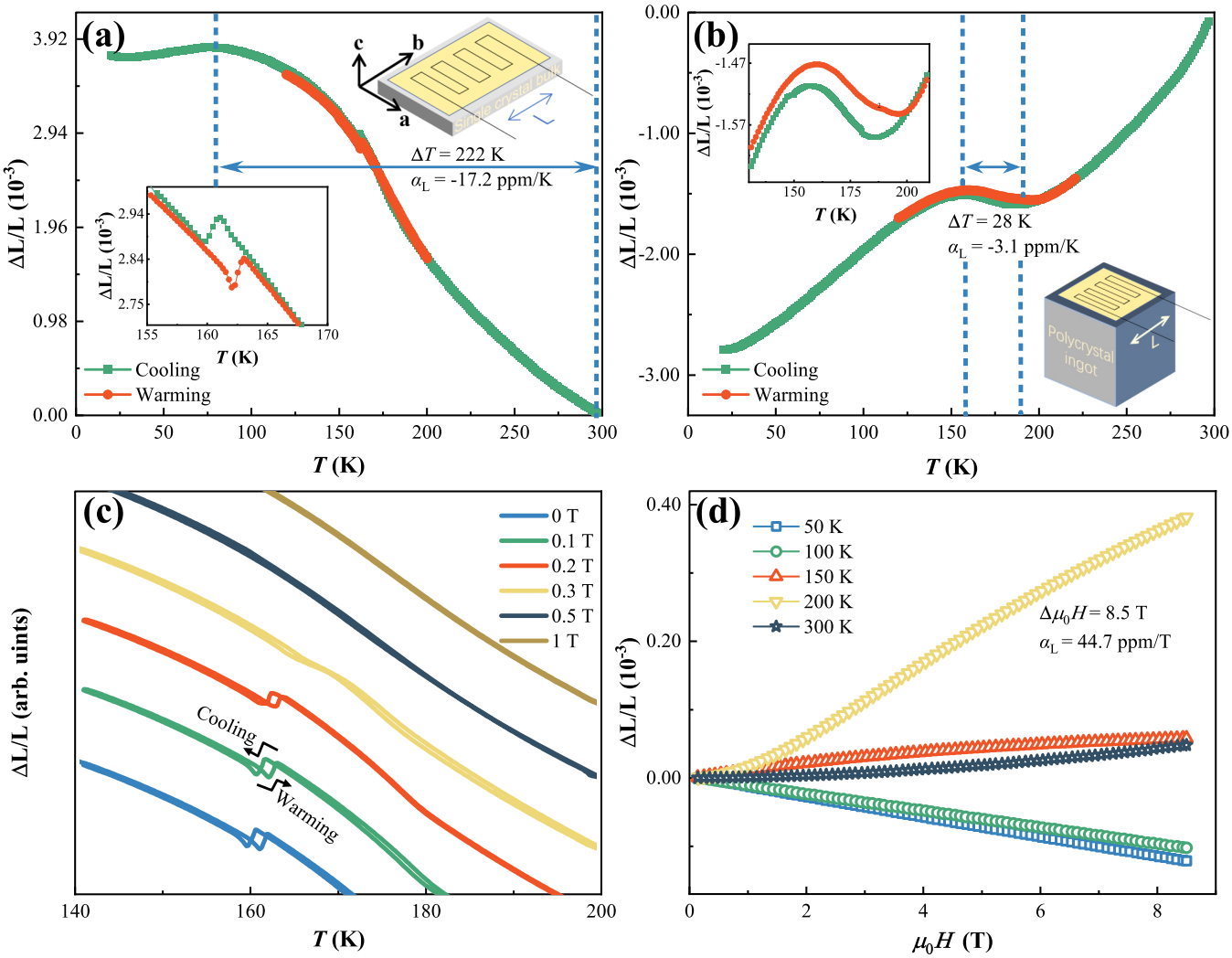

FIG. 5. (a) and (b) Linear thermal expansion $\Delta L/L$ (300 K) measurements for single-crystal and polycrystalline Cr_2Te_3, respectively. The average linear coefficient of thermal expansion α_L and related temperature span ΔT of NTE are marked. The red and green lines represent the heating and cooling processes, respectively, and the inset is an enlarged view near the transition temperature. (c) Temperature dependence of $\Delta L/L$ in different fields. (d) Field dependence of $\Delta L/L$ at different temperatures.

a wide temperature range from 70 to 300 K, leading to a large NTE coefficient $\alpha_L = -17.2$ ppm/K. For the polycrystal ingot sample, we ground single crystals and pressed them into blocks. As revealed in Fig. 5(b), it shrank gradually during cooling until it neared the phase transition zone at 160 K, followed by an expansion. The NTE coefficient of this polycrystal is around −3.1 ppm/K, while the volumetric coefficient of thermal expansion is $\alpha_V = 3\alpha_L = -9.3$ ppm/K, which is significantly different from the value obtained via XRD, −50 ppm/K. Given the significant density difference between the polycrystal and the single crystals, the crystal boundary may be a fundamental contributor to the variance [44,45]. Apart from this, we observe thermal hysteresis between the cooling and warming curves, shown in the insets in Figs. 5(a) and 5(b), which provides further direct evidence of the presence of first-order phase transition. By analogy, the intrinsic correlation between the NTE behavior and magnetism in CrTe compounds was analyzed in detail, possibly originating from the magnetovolume effect [46].

We have also explored the evolution of lattice distortion under an applied field. In Figs. 5(c) and 5(d), the thermal hysteresis is notable for $\mu_0 H = 0$, 0.1, and 0.2 T and shifts gradually to a higher temperature as the field strength increases. The hysteresis is strongly suppressed for $\mu_0 H = 0.3$ T and eventually disappears when $\mu_0 H \geqslant 0.5$ T, indicating that the lattice distortion and the related first-order phase transition are suppressed by the field. The effect of an external magnetic field on the first-order phase transition is evidence of a strong SLC, which usually results in a strong magnetostriction. In Fig. 5(d), we find the magnetostriction coefficient is negative at low temperature and changes sign when the temperature exceeds 150 K. The maximum magnetostriction coefficient of 44.7 ppm/T is found at 200 K due to the strong SLC.

The magnetic ground-state properties of the Cr_2Te_3 single crystal were calculated from first principles. We first study the magnetic coupling between the Cr atoms by considering five different magnetic structure configurations in a unit cell, including two FM configurations, one ferrimagnetic configuration, and two AFM configurations, as demonstrated in

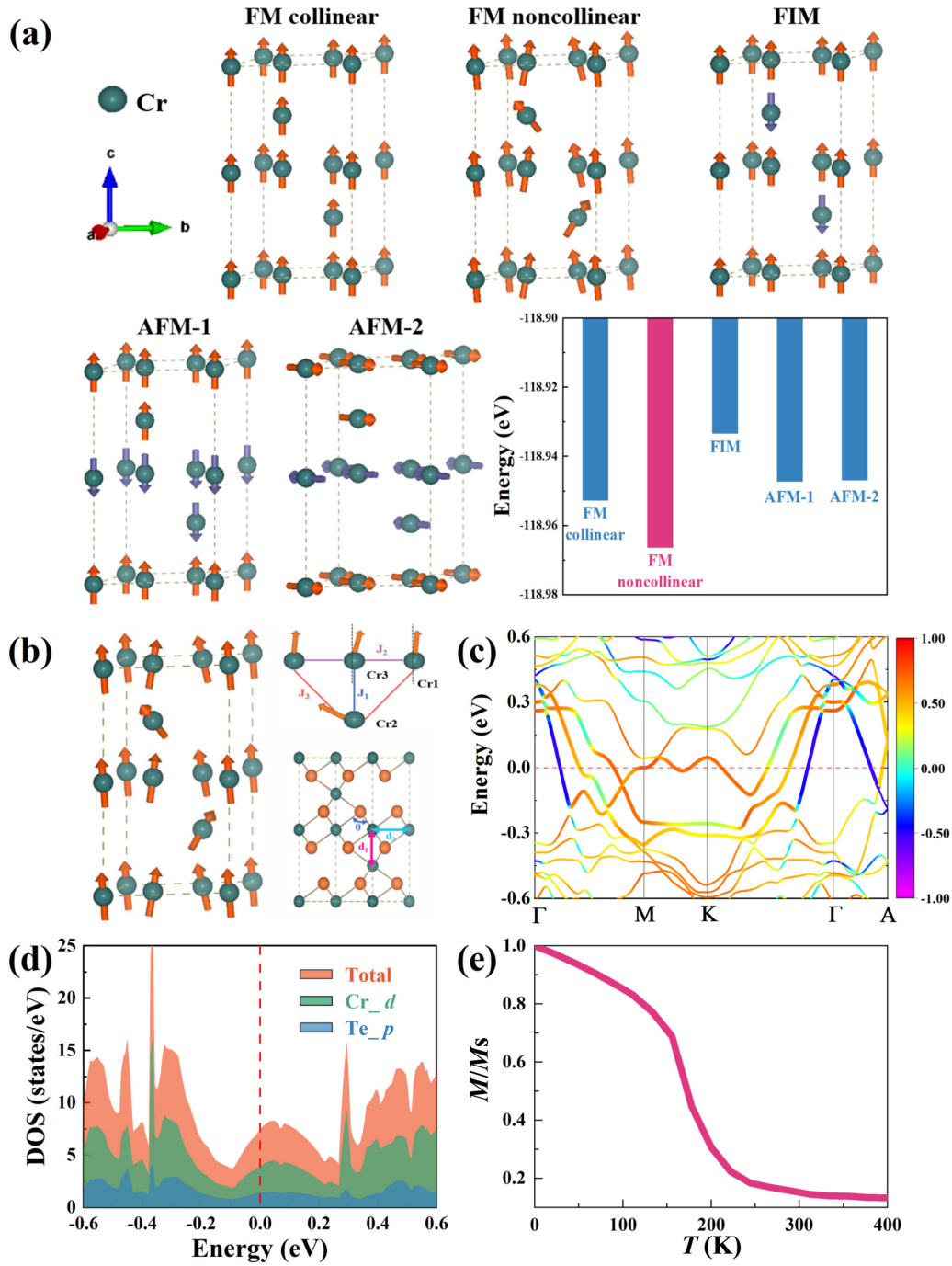

FIG. 6. (a) Comparison of possible magnetic structures and their individual total energies. (b) Magnetic structures and magnetic exchange interactions of Cr_2Te_3. (c) and (d) Energy band structure and partial density of states (PDOS) diagrams of Cr_2Te_3. (e) Monte Carlo simulation of the normalized magnetic moment of bulk Cr_2Te_3 as a function of temperature.

Fig. 6(a). We find that the canted FM structure has the lowest energy. In this low-energy configuration, the magnetic moments have large out-of-plane components aligned parallel to the c axis and small in-plane components aligned antiparallel to the diagonal of ab plane, consistent with our measurements of magnetic properties. The side view of the intercalated layers shows that Cr1, Cr2, and Cr3 moments have different canting angles away from the c direction. The moments of intercalated Cr2 atoms have the stronger canting, and the canting angles of Cr1 and Cr3 moments are small. This is qualitatively consistent with the previous calculation of magnetic structure of Cr_2Te_3 [47].

Figure 6(c) shows the calculated band structure of Cr_2Te_3 in the low-energy canted FM configuration, where the different colors denote the z component of the spins S_z of the bands. We find that most bands crossing the Fermi level carry positive S_z, signifying metallic FM behavior. There are bands with small S_z components due to the canted magnetic configuration. In Fig. 6(d), the calculated density of the states suggests that the bands near the Fermi level are largely contributed by

the Cr d and Te p orbitals. The strong hybridization between the Cr d and Te p orbitals may result in an indirect exchange interaction between the two Cr moments mediated by the neighboring Te atom [48].

We attempt to explain the magnetic mechanism by analyzing the interlayer and intralayer exchange coupling parameters. The distance between the neighboring Cr atoms within the layers is a relatively large value of 3.93 Å, therefore weakening their direct exchange interaction [44]. In contrast, the bond angles of Cr-Te-Cr within the layers are about 92.3°, resulting in a superexchange which favors the FM arrangements. According to Goodenough-Kanamori-Anderson rules [49–51], the interlayer distance is 2.99 Å, and the magnetic interaction between Cr2 and Cr3 is expected to be stronger than the intralayer Cr moments. The calculated exchange coupling parameters J_1, J_2, and J_3 are 13.665, 4.754, and 3.566 meV, respectively. Their positive values indicate that FM interactions dominate in the interlayer and intralayer coupling. Theoretical calculations give magnetic moment values of $3.019\mu_B$, $3.014\mu_B$, and $3.044\mu_B$ for Cr1, Cr2, and Cr3 respectively, consistent with the ionic model but all significantly higher than the empirical value of $2.56\mu_B$ for average Cr atoms [17]. Notably, the canted FM configuration we consider is just one possible low-energy magnetic configuration, and different energetically degenerate magnetic configurations may coexist in Cr_2Te_3; hence, the empirically measured magnetic moment would be the average of these configurations [52].

We also evaluate the Curie temperature of Cr_2Te_3 via Monte Carlo simulations with the Heisenberg model and using the magnetic parameters calculated above. The spin Hamiltonian based on a classical effective spin model is defined as [53,54]

$$H = -\frac{1}{2}\sum_{ij} J_{ij} S_i S_j - \frac{1}{2}\sum_{ij} B_{ij} S_i^Z S_j^Z + A\sum_i \left(S_i^Z\right)^2, \quad (3)$$

where S_i is the normalized spin vector on site i, J_{ij} and B_{ij} are the isotropic and anisotropic parts of the exchange interactions between sites i and j, respectively, and A is the magnetic anisotropy. As depicted in Fig. 6(e), we obtain T_C equal to 183 K, which is close to the experimental measurement. However, T_N is difficult to estimate since the DFT calculation could give the magnetic parameters only at 0 K and the positive exchange coupling parameters prohibited the AFM state. We did discover that J_2 and J_3 are small and can easily change signs due to the lattice volume change and distortions at high temperatures, hence the introduction of the AFM state.

Finally, we investigate the critical behavior to uncover the relationship between the magnetic field and the structure of Cr_2Te_3. Figure 7(a) illustrates the Arrott plots of M^2 versus H/M. All curves on the Arrott plots show linear behaviors in the high-field region, which suggests that the magnetic interaction in Cr_2Te_3 can be described by the conventional Landau mean-field model [55,56]. According to Banerjee's criterion, the phase transition is first order if the slope of $dM^2/d(H/M)$ is negative and second order if it is positive [57]. In our result, the slope changes from negative to positive in the low-field region, where the critical field strength is defined as H_C, as presented in the inset. The saturated field strength H_S can be

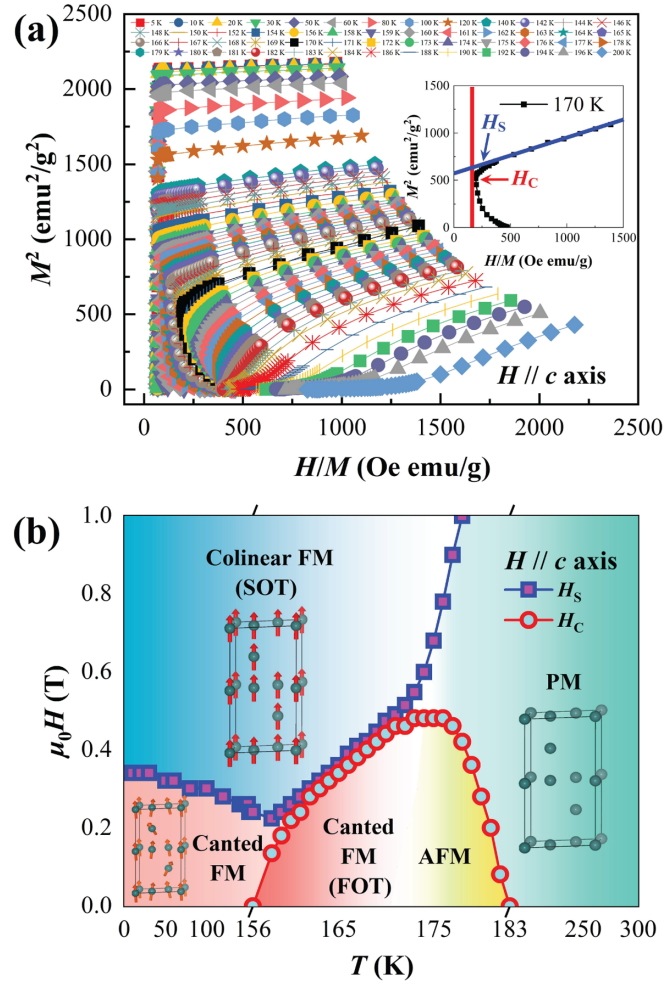

FIG. 7. (a) Arrott plots of M^2 versus H/M around T_C and T_N for Cr_2Te_3 (the curves at T_C and T_N are marked in red and blue, respectively). (b) H-T phase diagram obtained from the scaling relationship with $H \parallel c$ axis.

derived from the linear fit of the M^2 curves in the high-field region.

Based on this method, we construct a magnetic phase diagram of Cr_2Te_3 by connecting H_C and H_S points. As revealed in Fig. 7(b), we find that in low fields, Cr_2Te_3 has a canted FM state at low temperatures, an AFM state at moderate temperatures, and a PM state at high temperatures. A magnetic field stronger than H_S can transform these magnetic states to a collinear FM state where the magnetic moments tend to be parallel and constant. The AFM state shows a distinct bell shape, indicating that it is influenced by the combined effect of magnetic field and temperature. A magnetic field below the maximum critical field strength of 0.48 T sees a rich evolution of several magnetic states due to energy competition, whereby as the temperature increases, the canted or collinear FM state undergoes a first-order phase transition into the AFM state, then crosses the right boundary of the H_C curve with a second-order phase transition, and finally settles into a PM state. Only the FM-PM second-order phase transition is possible above $H_C = 0.48$ T.

IV. CONCLUSION

We grew Cr_2Te_3 single crystals via the self-flux method and systematically investigated their magnetic and electric properties. Two magnetic transitions coexisted in this system: FM-AFM ($T_C = 160$ K) and AFM-PM ($T_N = 181$ K). The FM transition was evidently more sensitive than the AFM transition. Raising the magnetic field strength greatly increased T_C while slightly lowering T_N. In a critical field of 0.48 T, the AFM orders disappeared, and the FM orders degenerated from the first order to the second order. Furthermore, we found that the lattice constant a or b of Cr_2Te_3 increases with decreasing temperature, with a significant NTE coefficient $\alpha_L = -17.2$ ppm/K. Raising the magnetic field strength also caused Cr_2Te_3 to positively expand, with a maximum rate of 44.7 ppm/T at 200 K. Bulk Cr_2Te_3 had a morphology tunable by an external magnetic field, and this property is expected to be present in its thin films as well, which hints at the feasibility of electric field modulation.

Analysis of Arrott plots revealed the relationship between the critical field strength and the transition temperature. The possible canted FM ground state was predicted from first principles; therefore, we finally obtained a complete phase diagram of the evolution of the ground state under the influence of magnetic fields. The results presented here have potential applications in the development of spintronics devices.

ACKNOWLEDGMENTS

This work was supported by the National Key Research and Development Program under Contract No. 2021YFA1600201; the National Natural Science Foundation of China under Contracts No. 11674326, No. 11874357, and No. 11904003; the Joint Funds of the National Natural Science Foundation of China; the Chinese Academy of Sciences' Large-Scale Scientific Facility under Contracts No. U1832141 and No. U1932217; the Key Research Program of Frontier Sciences, CAS (QYZDB-SSW-SLH015); the Excellence and Scientific Research Grant of the Hefei Science Center of CAS (2018HSC-UE011); and testing assistance from Shiyanjia Lab. The authors thank Prof. D. F. Shao from the Institute of Solid State Physics (CAS) for his assistance in editing the revised manuscript.

[1] N. D. Mermin and H. Wagner, Phys. Rev. Lett. **17**, 1133 (1966).
[2] B. Huang, G. Clark, E. Navarro-Moratalla, D. R. Klein, R. Cheng, K. L. Seyler, D. Zhong, E. Schmidgall, M. A. McGuire, D. H. Cobden, W. Yao, D. Xiao, P. Jarillo-Herrero, and X. D. Xu, Nature (London) **546**, 270 (2017).
[3] C. Gong, L. Li, Z. L. Li, H. W. Ji, A. Stern, Y. Xia, T. Cao, W. Bao, C. Z. Wang, Y. Wang, Z. Q. Qiu, R. J. Cava, S. G. Louie, J. Xia, and X. Zhang, Nature (London) **546**, 265 (2017).
[4] Y. J. Deng, Y. J. Yu, Y. C. Song, J. Z. Zhang, N. Z. Wang, Z. Y. Sun, Y. F. Yi, Y. Z. Wu, S. W. Wu, J. Y. Zhu, J. Wang, X. H. Chen, and Y. B. Zhang, Nature (London) **563**, 94 (2018).
[5] M. Bonilla, S. Kolekar, Y. J. Ma, H. C. Diaz, V. Kalappattil, R. Das, T. Eggers, H. R. Gutierrez, M. H. Phan, and M. Batzill, Nat. Nanotechnol. **13**, 289 (2018).
[6] W. Yu, J. Li, T. S. Herng, Z. S. Wang, X. X. Zhao, X. Chi, W. Fu, I. Abdelwahab, J. Zhou, J. D. Dan, Z. X. Chen, Z. Chen, Z. J. Li, J. Lu, S. J. Pennycook, Y. P. Feng, J. Ding, and K. P. Loh, Adv. Mater. **31**, 1903779 (2019).
[7] D. J. O'Hara, T. C. Zhu, A. H. Trout, A. S. Ahmed, Y. K. Luo, C. H. Lee, M. R. Brenner, S. Rajan, J. A. Gupta, D. W. McComb, and R. K. Kawakami, Nano Lett. **18**, 3125 (2018).
[8] T. Danz, Q. Liu, X. D. Zhu, L. H. Wang, S. W. Cheong, I. Radu, C. Ropers, and R. I. Tobey, J. Phys.: Condens. Matter **28**, 356002 (2016).
[9] H. Ipser, K. L. Komarek, and K. O. Klepp, J. Less-Common Met. **92**, 265 (1983).
[10] M. A. McGuire, V. O. Garlea, S. KC, V. R. Cooper, J. Yan, H. Cao, and B. C. Sales, Phys. Rev. B **95**, 144421 (2017).
[11] J. H. Zhang, T. L. T. Birdwhistell, and C. J. O'Connor, Solid State Commun. **74**, 443 (1990).
[12] J. Yan, X. Luo, G. T. Lin, F. C. Chen, J. J. Gao, Y. Sun, L. Hu, P. Tong, W. H. Song, Z. G. Sheng, W. J. Lu, X. B. Zhu, and Y. P. Sun, Europhys. Lett. **124**, 67005 (2019).
[13] Y. Liu, M. Abeykoon, E. Stavitski, K. Attenkofer, and C. Petrovic, Phys. Rev. B **100**, 245114 (2019).
[14] Z. Z. Jiang, X. Luo, J. Yan, J. J. Gao, W. Wang, G. C. Zhao, Y. Sun, J. G. Si, W. J. Lu, P. Tong, X. B. Zhu, W. H. Song, and Y. P. Sun, Phys. Rev. B **102**, 144433 (2020).
[15] L. Z. Zhang, A. L. Zhang, X. D. He, X. W. Ben, Q. L. Xiao, W. L. Lu, F. Chen, Z. J. Feng, S. X. Cao, J. C. Zhang, and J. Y. Ge, Phys. Rev. B **101**, 214413 (2020).
[16] F. Grönvold and E. F. Westrum, Z. Anorg. Allg. Chem. **328**, 272 (1964).
[17] A. F. Andresen, Acta Chem. Scand. **24**, 3495 (1970).
[18] S. Ohta, T. Kanomata, T. Kaneko, and H. Yoshida, J. Phys.: Condens. Matter **5**, 2759 (1993).
[19] K. Lasek, P. M. Coelho, P. Gargiani, M. Valvidares, K. Mohseni, H. L. Meyerheim, I. Kostanovskiy, K. Zberecki, and M. Batzill, Appl. Phys. Rev. **9**, 011409 (2022).
[20] D. C. Freitas, R. Weht, A. Sulpice, G. Remenyi, P. Strobel, F. Gay, J. Marcus, and M. Núñez-Regueiro, J. Phys.: Condens. Matter **27**, 176002 (2015).
[21] X. D. Sun *et al.*, Nano Res. **13**, 3358 (2020).
[22] Y. Wen, Z. H. Liu, Y. Zhang, C. X. Xia, B. X. Zhai, X. H. Zhang, G. H. Zhai, C. Shen, P. He, R. Q. Cheng, L. Yin, Y. Y. Yao, M. G. Sendeku, Z. X. Wang, X. B. Ye, C. S. Liu, C. Jiang, C. X. Shan, Y. W. Long, and J. He, Nano Lett. **20**, 3130 (2020).
[23] L. J. Meng, Z. Zhou, M. Q. Xu, S. Q. Yang, K. P. Si, L. X. Liu, X. G. Wang, H. N. Jiang, B. X. Li, P. X. Qin, P. Zhang, J. L. Wang, Z. Q. Liu, P. Z. Tang, Y. Ye, W. Zhou, L. H. Bao, H. J. Gao, and Y. J. Gong, Nat. Commun. **12**, 809 (2021).
[24] J. S. Chen, L. J. Wang, M. Zhang, L. Zhou, R. N. Zhang, L. P. Jin, X. S. Wang, H. L. Qin, Y. Qiu, J. W. Mei, F. Ye, B. Xi, H. T. He, B. Li, and G. Wang, Nano Lett. **19**, 6144 (2019).
[25] D. M. Burn, L. B. Duffy, R. Fujita, S. L. Zhang, A. I. Figueroa, J. Herrero-Martin, G. van der Laan, and T. Hesjedal, Sci. Rep. **9**, 10793 (2019).
[26] L. Zhou, J. S. Chen, X. B. Chen, B. Xi, Y. Qiu, J. W. Zhang, L. J. Wang, R. N. Zhang, B. C. Ye, P. B. Chen, X. X. Zhang, G. P. Guo, D. P. Yu, J. W. Mei, F. Ye, G. Wang, and H. T. He, ACS Appl. Mater. Interfaces **12**, 25135 (2020).

[27] B. Li, R. N. Zhang, L. Zhou, L. J. Wang, Z. J. Yan, H. T. He, and G. Wang, Appl. Phys. Lett. **120**, 093102 (2022).
[28] J. S. Chen, L. Zhou, L. J. Wang, Z. J. Yan, X. T. Deng, J. M. Zhou, J. W. Mei, Y. Qiu, B. Xi, X. S. Wang, H. T. He, and G. Wang, Cryst. Growth Des. **22**, 140 (2022).
[29] See Supplemental Material at http://link.aps.org/supplemental/10.1103/PhysRevB.106.094407 for component characterization, structure characterization, and magnetic entropy anisotropy.
[30] P. Hohenberg and W. Kohn, Phys. Rev. **136**, B864 (1964).
[31] G. Kresse and J. Hafner, Phys. Rev. B **47**, 558 (1993).
[32] G. Kresse and J. Furthmüller, Phys. Rev. B **54**, 11169 (1996).
[33] J. P. Perdew, K. Burke, and M. Ernzerhof, Phys. Rev. Lett. **77**, 3865 (1996).
[34] P. E. Blöchl, Phys. Rev. B **50**, 17953 (1994).
[35] G. Pizzi *et al.*, J. Phys.: Condens. Matter **32**, 165902 (2020).
[36] X. He, N. Helbig, M. J. Verstraete, and E. Bousquet, Comput. Phys. Commun. **264**, 107938 (2021).
[37] W. Bensch, O. Helmer, and C. Nather, Mater. Res. Bull. **32**, 305 (1997).
[38] A. L. Coughlin, D. Xie, Y. Yao, X. Zhan, Q. Chen, H. Hewa-Walpitage, X. H. Zhang, H. Guo, H. D. Zhou, J. Lou, J. Wang, Y. S. Li, H. A. Fertig, and S. X. Zhang, ACS Nano **14**, 15256 (2020).
[39] C. Kittel, *Introduction to Solid State Physics*, 8th ed. (Wiley, Hoboken, NJ, 2005).
[40] T. Hashimoto, K. Hoya, M. Yamaguchi, and I. Ichitsubo, J. Phys. Soc. Jpn. **31**, 679 (1971).
[41] K. Shimada, T. Saitoh, H. Namatame, A. Fujimori, M. Matoba, K. Hatakeyama, and S. Anzai, Jpn. J. Appl. Phys. **32**, 355 (1993).
[42] Y. H. Wang, J. Yan, J. B. Li, S. S. Wang, M. Song, J. P. Song, Z. H. Li, K. Chen, Y. L. Qin, L. S. Ling, H. F. Du, L. Cao, X. Luo, Y. M. Xiong, and Y. P. Sun, Phys. Rev. B **100**, 024434 (2019).
[43] M. Romanini, Y. X. Wang, K. Gürpinar, G. Ornelas, P. Lloveras, Y. Zhang, W. K. Zheng, M. Barrio, A. Aznar, A. Gràcia-Condal, B. Emre, O. Atakol, C. Popescu, H. Zhang, Y. Long, L. Balicas, J. Lluís Tamarit, A. Planes, M. Shatruk, and L. Mañosa, Adv. Mater. **33**, 2008076 (2021).
[44] X. L. Wang, P. Tong, J. C. Lin, X. K. Zhang, C. Yang, Z. C. Wang, M. Wang, Y. Wu, L. Zhang, W. Tong, W. H. Song, and Y. P. Sun, J. Alloys Compd. **862**, 158616 (2021).
[45] K. Takenaka, Front. Chem. **6**, 267 (2018).
[46] J. W. Xu, X. Q. Zheng, S. X. Yang, L. Xi, S. G. Wang, L. Zhang, W. Y. Yang, J. B. Yang, X. B. Ma, D. F. Chen, L. H. He, S. H. Deng, J. Y. Zhang, Y. F. Wu, and B. G. Shen, Inorg. Chem. **59**, 8603 (2020).
[47] M. Y. Bian, A. N. Kamenskii, M. J. Han, W. J. Li, S. C. Wei, X. Z. Tian, D. B. Eason, F. Sun, K. K. He, H. L. Hui, F. Yao, R. Sabirianov, J. P. Bird, C. L. Yang, J. W. Miao, J. H. Lin, S. A. Crooker, Y. L. Hou, and H. Zeng, Mater. Res. Lett. **9**, 205 (2021).
[48] X. W. Zhang, B. Wang, Y. L. Guo, Y. H. Zhang, Y. F. Chen, and J. L. Wang, Nanoscale Horiz. **4**, 859 (2019).
[49] J. B. Goodenough, Phys. Rev. **100**, 564 (1955).
[50] J. Kanamori, J. Phys. Chem. Solids **10**, 87 (1959).
[51] P. W. Anderson, Phys. Rev. **115**, 2 (1959).
[52] S. J. Youn, S. K. Kwon, and B. I. Min, J. Appl. Phys. **101**, 09G522 (2007).
[53] S. Li, S. S. Wang, B. Tai, W. K. Wu, B. Xiang, X. L. Sheng, and S. A. Yang, Phys. Rev. B **103**, 045114 (2021).
[54] L. Liu, S. S. Chen, Z. Z. Lin, and X. Zhang, J. Phys. Chem. Lett. **11**, 7893 (2020).
[55] A. Arrott, Phys. Rev. **108**, 1394 (1957).
[56] S. N. Kaul, J. Magn. Magn. Mater. **53**, 5 (1985).
[57] B. K. Banerjee, Phys. Lett. **12**, 16 (1964).